

A Comprehensive View of the 13 December 2006 CME: From the Sun to Interplanetary Space

Y. Liu^{1,2}, J. G. Luhmann¹, P. C. Schroeder¹, L. Wang¹, Y. Li¹, R. P. Lin¹, S. D. Bale¹, R. Müller-Mellin³, M. H. Acuña⁴, and J.-A. Sauvaud⁵

ABSTRACT

The biggest halo coronal mass ejection (CME) since the Halloween storm in 2003, which occurred on 13 December 2006, is studied in terms of its solar source and heliospheric consequences. The CME is accompanied by an X3.4 flare, EUV dimmings and coronal waves. It generated significant space weather effects such as an interplanetary shock, radio bursts, major solar energetic particle (SEP) events, and a magnetic cloud (MC) detected by a fleet of spacecraft including STEREO, ACE, Wind and Ulysses. Reconstruction of the MC with the Grad-Shafranov (GS) method yields an axis orientation oblique to the flare ribbons. Observations of the SEP intensities and anisotropies show that the particles can be trapped, deflected and reaccelerated by the large-scale transient structures. The CME preceding shock is also observed at Ulysses which is 74° south of the Earth, indicative of a surprisingly large latitudinal extent of the shock. The shock arrival time at Ulysses is well predicted by an MHD model which can propagate the 1 AU data outward. The CME/shock is tracked remarkably well from the Sun all the way to Ulysses by coronagraph images, type II frequency drift, in situ measurements and the MHD model. These results reveal a technique combining MHD propagation of the solar wind and type II emissions to predict the shock arrival time at the Earth, important for space weather forecasting especially when in situ data are available from the Solar Orbiter and Sentinels.

Subject headings: shock waves — solar-terrestrial relations — solar wind — Sun: coronal mass ejections — Sun: radio radiation — Sun: particle emission

¹Space Sciences Laboratory, University of California, Berkeley, CA 94720, USA; liuxying@ssl.berkeley.edu.

²State Key Laboratory of Space Weather, Chinese Academy of Sciences, Beijing 100080, China.

³Institut für Experimentelle und Angewandte Physik, Universität Kiel, Kiel, Germany.

⁴NASA Goddard Space Flight Center, Greenbelt, Maryland, USA.

⁵Centre d'Etude Spatiale des Rayonnements, Centre National de la Recherche Scientifique, Toulouse, France.

1. Introduction

Coronal mass ejections (CMEs) are the most spectacular eruptions in the solar atmosphere and have been recognized as primary drivers of interplanetary disturbances. They are called interplanetary CMEs (ICMEs) when they move into the solar wind. Often associated with CMEs and ICMEs are radio bursts, shock waves, solar energetic particle (SEP) events, and prolonged southward magnetic field components. A southward field component can reconnect with geomagnetic fields and produce storms in the terrestrial environment (e.g., Dungey 1961). Understanding CMEs and characterizing their interplanetary transport are crucial for space weather forecasting but require coordinated multi-wavelength observations in combination with in situ measurements.

The 13 December 2006 CME is the largest halo CME since the Halloween storm which occurred in October - November 2003 (e.g., Gopalswamy et al. 2005; Richardson et al. 2005; Lario et al. 2005). It is also the largest CME in the STEREO era up to the time of writing. Different from the Halloween storm, this event is relatively isolated from other CMEs, so contamination by or mixing with other events is less pronounced; propagation into a solar wind environment near solar minimum would also make theoretical modeling easier. Accompanied by an X3.4 solar flare, the CME produced significant space weather effects including SEP events, an interplanetary shock, radio bursts and a magnetic cloud (MC) detected by various instruments aboard a fleet of spacecraft. Examining evolution and propagation of this event through the heliosphere would provide benchmark studies for CMEs, associated phenomena and space weather.

The purpose of this work is to study the solar source and heliospheric consequences of this CME in the frame of the Sun-Earth connection. We combine EUV, coronagraph, radio, in situ particle, plasma and magnetic field measurements with modeling efforts in an attempt to give a comprehensive view of the event; particular attention is paid to tracking the CME/shock all the way from the Sun out to interplanetary space. We look at EUV and coronagraph images in §2. Evolution of the CME in the heliosphere and its effects on particle transport are investigated in §3. In §4, we combine different data and demonstrate how the CME/shock propagation can be tracked using coordinated observations and MHD modeling. The results are summarized in §5.

2. CME at the Sun

STEREO/SECCHI was not turned on at the time of the CME, so we look at CME observations from LASCO and coronal observations from EIT aboard SOHO. Figure 1 dis-

plays combined images as seen by EIT and LASCO/C2 during the CME times. The CME starts with a mass flow in the southwest quadrant at 02:30 UT, coincident with a strong EUV brightening. Around 02:54 UT, it forms a nearly complete halo; the EUV brightening is followed by a dimming which quickly spreads into a large area of the solar disk. The CME moves further out around 03:06 UT and forms a spectacular ring of dense material with a bright feature embedded in the dark cavity trailing behind the ring. The EUV dimming area is now rather diffusive and almost covers the whole solar disk. The good timing between the dimming and CME indicates that the reduced EUV brightness results from removal of the coronal plasma due to the lift-off of the CME (e.g., Thompson et al. 1998; Zarro et al. 1999). Depletion of the coronal material by CMEs is possible if the associated magnetic field is opened or stretched into interplanetary space as proposed by many CME models.

Note that faint diffuse EUV brightenings are also seen and appear to be propagation fronts of the dimming. These brightenings may represent coronal waves propagating away from the active region; they were first found from EIT images and have been referred to as “EIT waves” for that reason (e.g., Thompson et al. 1998). The low cadence rate of EIT observations (12 min for the 195 Å band) does not allow an accurate determination of the speed of the waves. The brightenings moving toward the northeast hemisphere, however, seem to have a constant speed: they travel a distance of $\sim 0.86 R_{\odot}$ (solar radius) within 24 min from 02:24 UT to 02:48 UT and another $0.43 R_{\odot}$ within 12 min from 02:48 UT to 03:00 UT (see Figure 1). The speed is estimated to be about 420 km s^{-1} . The CME speed projected on the sky is about 1774 km s^{-1} as measured along a position angle of 193° (counter clockwise from the north; see CME identification and parameters at the LASCO CME catalogue <http://cdaw.gsfc.nasa.gov>), significantly larger than the EIT wave speed. It is not clear about the nature or origin of the coronal waves, although an unambiguous correlation between EIT waves and CMEs has been established (e.g., Biesecker et al. 2002).

The CME is accompanied by an X3.4 solar flare located in the active region NOAA 10930 (S06°W23°). The flare seems to be induced by strong shear in the magnetic field associated with a filament eruption, leading to two large ribbons which are twisted but largely horizontal around the filament channel (e.g., Zhang et al. 2007; Kosovichev & Sekii 2007). We will compare the orientation of the filament channel with reconstruction of the associated MC observed in situ (see §3.1; also see Li et al. 2007)

3. Interplanetary Consequences

After the abrupt formation in the solar corona, the CME propagates into the interplanetary medium and is observed in situ by STEREO, ACE and Ulysses. We infer the ICME

structure from in situ measurements of plasma and magnetic field parameters combined with a flux-rope reconstruction model. Connectivity of the ICME back to the Sun is indicated by energetic particles which could be channeled, constrained and reaccelerated by the transient structure.

3.1. ICME at 1 AU

STEREO observed the ICME after an exit from the terrestrial magnetosheath. Figure 2 shows the in situ measurements across the event from SWEA (Sauvaud et al. 2007) and MAG (Acuña et al. 2007) of STEREO/IMPACT (Luhmann et al. 2007). STEREO A and B were not separated, so they observed essentially the same structure. The plasma parameters (e.g., density, velocity and temperature) are not available from STEREO for that time period. Bi-directional streaming electrons (BDEs) seem coincident with the strong magnetic fields, indicative of closed field lines within the event; rotation of the field (see the field elevation angle) indicates an MC. The MC interval is determined from the BDEs but also consistent with the reduced field variance and the rotation of the field. The magnetic field has a significant negative (southward) component which caused a major geomagnetic storm with $D_{st} \sim -190$ nT. Interestingly, there is a current sheet (indicated by the peak of the field elevation angle) within the MC, which might be due to the passage of the comet McNaught through the event (C. T. Russell, private communication). The magnetic field trailing behind the MC has a roughly constant direction, presumably stretched by the MC because of its large speed. A preceding shock, as can be seen from simultaneous increases in the electron flux and magnetic field strength, passed the spacecraft at 14:38 UT on December 14. The transit time is about 36 hr from the Sun to the Earth, suggesting an average speed of ~ 1160 km s⁻¹. This speed is significantly smaller than the white-light speed close to the Sun (1774 km s⁻¹) but larger than the shock speed at 1 AU (1030 km s⁻¹; see below), so the shock must be decelerated as the high speed flow overtakes the preceding solar wind. Propagation of the shock as well as the deceleration is calculated in §4.

Complementary plasma parameters from ACE are displayed in Figure 3; the magnetic field is almost the same as measured at STEREO. The ICME interval is identified by combining the enhanced helium/proton density ratio and depressed proton temperature (as compared with the normal temperature expected from the observed speed); the boundaries also agree with the discontinuities in the density, bulk speed and magnetic field. The resulting radial width (average speed times the duration) is about 0.67 AU; the MC indicated by STEREO BDEs is about the first half of the time interval. The preceding shock is also apparent from the plasma parameters. The shock speed is about 1030 km s⁻¹ as calculated

from the conservation of mass across the shock. As shown above, the shock has to be decelerated when propagating from the Sun to the Earth. A least squares fit of the plasma and magnetic field data across the shock to the Rankine-Hugoniot relations (Viñas & Scudder 1986) gives a shock normal with elevation angle $\theta \simeq -12.7^\circ$ and azimuthal angle $\phi \simeq 308^\circ$ in RTN coordinates (with \mathbf{R} pointing from the Sun to the spacecraft, \mathbf{T} parallel to the solar equatorial plane and along the planet motion direction, and \mathbf{N} completing the right-handed system). The shock normal makes an angle of about 56° with the upstream magnetic field, so the shock may be quasi-perpendicular. Liu et al. (2006a) find that the sheath regions between fast ICMEs and their preceding shocks are analogous to planetary magnetosheaths and often characterized by plasma depletion layers and mirror-mode waves. The proton density in the sheath of the current event first increases and then decreases quickly close to the MC, very similar to the case shown in their Figure 3. Magnetic fluctuations in the sheath appear consistent with mirror-mode waves but note that large depressions are due to current sheet crossings; a quasi-perpendicular shock would heat the plasma preferentially in the direction perpendicular to the field, so the plasma downstream of the shock may be unstable to the mirror-mode instability (e.g., Liu et al. 2007). There seems another ICME on December 17 as can be seen from the low proton temperature and declining speed. Interactions between the two events are likely present.

We reconstruct the MC structure using the Grad-Shafranov (GS) technique which includes the thermal pressure and can give a cross section without prescribing the geometry (e.g., Hau & Sonnerup 1999; Hu & Sonnerup 2002). This method relies on the feature that the thermal pressure and the axial magnetic field depend on the vector magnetic potential only (Schindler et al. 1973; Sturrock 1994), which has been validated by observations from STEREO and ACE/Wind when these spacecraft are well separated (Liu et al. 2008). We apply the method to the plasma and magnetic field data between 22:48 UT on December 14 (the MC leading edge) and 04:34 UT on December 15 (right before the current sheet within the MC) when the magnetic field has the clearest rotation. All the data used in the reconstruction are from the MC interior. The reconstruction results are illustrated in Figure 4. The recovered cross section (in a flux-rope frame with \mathbf{x} along the spacecraft trajectory and \mathbf{z} in the direction of the axial field) shows nested helical field lines, suggestive of a flux-rope structure. The spacecraft (ACE and STEREO) seem to cross the MC close to the axis with an impact parameter of 0.01 AU; the maximum axial field is also very close to the leading edge ($x = 0$). The transverse fields along the spacecraft path indicate a left-handed chirality. The reconstruction gives an axis elevation angle $\theta \simeq -57^\circ$ and azimuthal angle $\theta \simeq 261^\circ$ in RTN coordinates, as shown in Figure 4 (right). Since the axial field points southward and the field configuration is left-handed, a spacecraft would see a field which is first most negative and then becomes less negative as the MC passes the spacecraft along the radial

direction. These results are consistent with observations (see Figures 2 and 3). We also apply the method to a larger interval inside the MC (with the current sheet excluded) and obtain a similar cross section and axis orientation. Note that the axis orientation is oblique to the filament channel; similar results are obtained for other cases (e.g., Wang et al. 2006). The MC axis orientation depends on which part of the CME is observed in situ, or the CME possibly rotates during the propagation in the heliosphere.

3.2. SEP Events

Major SEP events are observed at 1 AU in association with the X3.4 flare and the ICME-driven shock. The ICME structure as well as its effects on energetic particle transport can also be inferred from particle measurements. Figure 5 shows the particle intensities measured by ACE/EPAM and STEREO A/SEPT. Four particle onsets are evident. The timing with the flares and shocks indicates that the first particle enhancement is associated with the injection from the X3.4 flare (02:38 UT on December 13), the second one associated with the ICME forward shock (14:38 UT on December 14), the third one with an X1.5 flare (22:14 UT on December 14) which occurred in the same active region (NOAA 10930; S06°W46°), and the fourth one with the shock downstream of the ICME (17:23 UT on December 16; see Figures 2 and 3). The X3.4 flare produced an intense electron flux which declines during a long time period; velocity dispersion is not clear in the electrons but present in the protons. The ICME preceding shock continues to accelerate protons to \sim MeV energies at 1 AU but appears to have a small effect on the electrons, probably because the electron enhancement at the shock is masked by the large preshock intensities. There is an apparent exclusion of the protons from the ICME interior (see second panel), presumably screened off by the strong fields within the ICME; the proton signature also seems consistent with the BDE interval. Interestingly, there is an intensity enhancement of the electrons within the ICME due to the X1.5 flare; it is likely that the electrons stream along the field line from the active region and are trapped inside the ICME (e.g., Kahler & Reames 1991; Larson et al. 1997), so the ICME may still be magnetically connected to the Sun. These features are very similar to the observations during the Halloween storm (e.g., Malandraki et al. 2005; McKibben et al. 2005).

The two bottom panels in Figure 5 show anisotropy information of the particles provided by STEREO A/SEPT. SEPT has two separate telescopes with one looking in the ecliptic plane along the nominal Parker spiral field toward and away from the Sun and the other looking vertical to the plane toward the south and north, respectively (Müller-Mellin et al. 2007). The lines in the two panels represent the intensity differences between the two di-

rections for each telescope (i.e., differences between south and north and between the two opposite directions along the Parker field); the intensity difference is normalized by $4000 \text{ cm}^{-2} \text{ s}^{-1} \text{ sr}^{-1} \text{ MeV}^{-1}$ for the electrons and $1000 \text{ cm}^{-2} \text{ s}^{-1} \text{ sr}^{-1} \text{ MeV}^{-1}$ for the protons. The data before 18:10 UT on December 14 are discarded, because the SEPT doors were closed since the launch of STEREO and were opened one by one from 17:32 UT to 18:10 UT on December 14. Anisotropy information is thus not available for the particles from the X3.4 flare the ICME preceding shock. The X1.5 flare produced electrons and protons moving largely anti-sunward at 1 AU, but some anti-sunward particles may be mirrored back by the enhanced magnetic fields in the ICME/sheath and then propagate in the sunward direction. A beam of particles accelerated at the second shock, which may also be deflected by the first ICME, move sunward and northward.

Further information about the electron behaviors across the ICME is provided by SWEA (Sauvaud et al. 2007) and STE D2 (one of the detectors looking away from the Sun; see Lin et al. 2008) on board STEREO as shown in Figure 6. The electron energies range from $\sim 1 \text{ eV}$ to 100 keV . The pitch angle distribution of 247 eV electrons displayed in Figure 2 is measured by SWEA in the spacecraft frame; BDE signatures are discernible from $\sim 50 \text{ eV}$ to $\sim 1.7 \text{ keV}$ for this event. At the ICME-driven shock, velocity dispersion is present in the low-energy electrons but less evident in the high-energy electrons. There seems a flux decrease associated with the BDE interval; the high-energy electrons from STE recover before the trailing edge of the BDE interval, earlier than the low-energy electrons. The electron intensity profiles are quantitatively different from what is shown in Figure 5, which may be due to different looking directions of the detectors and different connectivity of the spacecraft via the magnetic field line to the Sun.

The above results suggest that the particle transport is largely governed by the large-scale transient structures. The particles can be deflected, constrained, and reaccelerated by ICMEs and associated shocks, so modeling of the particle transport is complicated by the presence of these structures. The energetic particles, however, could be used to trace the ICME structure, which can then be compared with plasma and magnetic field measurements. More information on ion intensities, spectra, and composition regarding the event can be found in Mewaldt et al. (2007) and Mulligan et al. (2007).

3.3. ICME at Ulysses and Beyond

Ulysses was at a distance 2.73 AU , latitude -74.9° and longitude 123.3° in the heliographic inertial system when it observed a large shock at 17:02 UT on December 17. Ulysses was about 117° east and 74° south of the Earth. Figure 7 displays the Ulysses data for a

5-day interval. During this time period, there are no clear ICME signatures such as enhanced helium abundance, depressed proton temperature, and smooth strong magnetic fields compared with the ambient solar wind upstream of the shock. It is likely that the ICME is missed at Ulysses whereas the shock is observed. The shock has a speed about 870 km s^{-1} , smaller than the 1 AU speed (1030 km s^{-1}) but not significantly. Given a speed difference larger than 740 km s^{-1} between at the Sun and 1 AU, the primary deceleration of the shock must occur within 1 AU, and further out the shock moves with a roughly constant speed. Propagation of the shock from the Sun to Ulysses is quantified in §4 by combining the coronagraph, radio, and in situ data with an MHD model. The shock normal has an elevation angle $\theta \simeq -38.3^\circ$ and azimuthal angle $\phi \simeq 77.5^\circ$ (RTN), resulting from the Rankine-Hugoniot calculations (Viñas & Scudder 1986). The angle between the shock normal and the upstream magnetic field is about 68° , so the shock is also quasi-perpendicular at Ulysses.

To show that Ulysses observed the same shock as ACE/STEREO, we propagate the solar wind data outward from 1 AU using an MHD model (Wang et al. 2000). The model has had success in connecting solar wind observations at different spacecraft (e.g., Wang et al. 2001; Richardson et al. 2002, 2005, 2006; Liu et al. 2006b). The model assumes spherical symmetry (1D) since we have solar wind measurements at only a single point. We use the solar wind parameters observed at 1 AU (50 days long around the ICME) as input to the model and propagate the solar wind outward. Figure 8 shows the observed speeds at 1 AU and Ulysses and the model-predicted speeds at certain distances. Small streams smooth out due to stream interactions as can be seen from the traces, but the large stream associated with the shock persists out to Ulysses. The predicted arrival time of the shock at Ulysses is only about 3.6 hr earlier than observed. The time difference is negligible compared with the propagation time of ~ 75.1 hr from ACE to Ulysses. The ambient solar wind predicted by the model is slower than observed at Ulysses, which is reasonable since Ulysses is at the south pole (74° south of ACE). Given the good stream alignment, we think that Ulysses and the near-Earth spacecraft observed the same shock. The successful model-data comparison also indicates that the shock surface is more or less spherical. It is reasonably surprising that the shock has a latitudinal extent larger than 74° ; spacecraft configured as above (i.e., one close to the solar equatorial plane and the other at the pole) are rare while they observe the same shock. Note that the longitudinal size of the shock is also large with a lower limit of 117° (the longitudinal separation between the Earth and Ulysses).

The large size of the shock indicates that the global configuration of the solar wind can be altered as the CME sweeps through the heliosphere. We also propagate the solar wind to large distances using the MHD model. The peak solar wind speeds quickly decrease as the high-speed flow interacts with the ambient medium. They are reduced to 630 km s^{-1} at 10 AU and to 490 km s^{-1} (close to the ambient level) by 50 AU. Therefore, the high-speed

streams would not produce significant effects at large distances.

4. CME/Shock Propagation

Of particular interest for space weather forecasting is the CME/shock propagation in the inner heliosphere. In the absence of observations of plasma features, propagation of shocks within 1 AU can be characterized by type II radio emissions (e.g., Reiner et al. 2007). Type II radio bursts, typically drifting downward in frequency, are remote signatures of a shock moving through the heliosphere and driving plasma radiation near the plasma frequency and/or its second harmonic (e.g., Nelson & Melrose 1985; Cane et al. 1987). The frequency drift results from the decrease of the plasma density as the shock propagates away from the Sun. The plasma frequency, f_p (kHz) = $8.97\sqrt{n \text{ (cm}^{-3}\text{)}}$, can be converted to a heliocentric distance r by assuming a density model $n = n_0/r^2$

$$r \text{ (AU)} = \frac{8.97\sqrt{n_0 \text{ (cm}^{-3}\text{)}}}{f_p \text{ (kHz)}}, \quad (1)$$

where n_0 is the plasma density at 1 AU. The height-time profile of shock propagation can then be obtained from the frequency drift.

Figure 9 displays the dynamic spectrum as well as soft X-ray flux associated with the CME. An intense type III radio burst occurred at about 02:29 UT on December 13 (Day 347), coincident with the peak of the X-ray flux. Type III bursts are produced by near-relativistic electrons escaping from the flaring site (e.g., Lin et al. 1973), so they drift very rapidly in frequency and appear as almost vertical features in the dynamic spectrum. Such an intense type III burst often indicates a major CME (Reiner et al. 2001). Note that many short-lived type III-like bursts are also seen starting from 17:00 UT on December 13; they are known as type III storms and presumably associated with a series of small electron beams injected from the Sun. Diffuse type II emissions occur at the fundamental and harmonic plasma frequencies and appear as slowly drifting features. They start from the type III burst and seem disrupted during the small flares around 13:00 UT on December 13 (see the X-ray flux). It is not clear whether the type II emissions after 16:00 UT on December 13 are at the fundamental or harmonic of the plasma frequency; the broad band may result from merging of the two branches. Apparently it is difficult to measure the frequency drift from individual frequencies associated with the type II bursts. An overall fit combined with in situ measurements at 1 AU would give a more accurate estimate for the height-time profile.

We employ a kinematic model to characterize the CME/shock propagation, similar to the approach of Gopalswamy et al. (2001) and Reiner et al. (2007). The shock is assumed

to start with an initial speed v_0 and a constant deceleration a lasting for a time period t_1 , and thereafter it moves with a constant speed v_s . The shock speed v_s and transit time t_T are known from 1 AU measurements, leaving only two free parameters in the model (a and t_1). At a time t , the distance of the shock can be expressed as

$$r = \begin{cases} d + v_s(t - t_T) + a(\frac{1}{2}t^2 + \frac{1}{2}t_1^2 - t_1t) & t < t_1 \\ d + v_s(t - t_T) & t \geq t_1 \end{cases} \quad (2)$$

where $d = 1$ AU and $v_0 = v_s - at_1$. The trace of the fundamental branch of the type II bursts is singled out using an interactive program and shown in Figure 10; the selected frequencies are converted to heliocentric distances using equation (1). We adjust the density scale factor n_0 to obtain a best fit of the frequency drift; a value of $n_0 \simeq 13 \text{ cm}^{-3}$, comparable to the plasma density in the ICME sheath (see Figure 3), gives a height-time profile that simultaneously matches the radio data and the shock parameters at 1 AU. Two curves corresponding to the emissions at the fundamental and harmonic plasma frequencies are obtained from the best fit, as shown in Figure 9. The fit is forced to be consistent with the overall trend of the frequency-drifting bands; discrepancies are seen at some times due to irregularities of the type II emissions. Note that the best fit yields the radial kinematic parameters of the CME/shock propagation with projection effects minimized. The radial velocity of the shock near the Sun given by the best fit is $v_0 \simeq 2212 \text{ km s}^{-1}$, larger than the measured CME speed projected onto the sky (1774 km s^{-1}). The deceleration is about -34.7 m s^{-2} , lasting for ~ 9.5 hr which corresponds to a distance of about 0.36 AU. Thereafter the shock moves with a constant speed 1030 km s^{-1} as measured at 1 AU.

In order to show how well the CME/shock is tracked by the fit, we extend the curve to the distance of Ulysses and plot in Figure 10 the CME locations measured by LASCO (see the LASCO CME catalogue at <http://cdaw.gsfc.nasa.gov>), the MHD model output of the shock arrival times every 0.2 AU between 1 - 2.6 AU, and the shock arrival time at Ulysses. The fit agrees with the LASCO data, the MHD model output at different distances and finally the Ulysses measurement. Note that we only use the type II frequency drift and the 1 AU shock parameters to obtain the height-time profile. Even at large distances the shock is still tracked remarkably well by the fit. The agreement verifies the kinematic model for the CME/shock propagation; a value of 2212 km s^{-1} should be a good estimate of the CME radial velocity near the Sun.

These results present a useful technique for space weather forecasting, especially when in situ measurements closer to the Sun are available (say, from the Solar Orbiter and Sentinels). In situ data closer to the Sun can be propagated to 1 AU by an MHD model; further constraints on the height-time profile are provided by the frequency drift of type II emissions. The advantage of this method is that the shock can be tracked continuously from the Sun all

the way to 1 AU; the arrival time of CME-driven shocks at the Earth can be predicted with an accuracy less than a few hours \sim days before they reach the Earth. Implementation of the method, specifically combining MHD propagation of the solar wind with type II frequency drift, is expected to be a routine possibility in the future when in situ data are available from the Solar Orbiter and Sentinels.

5. Summary

We have investigated the evolution and propagation of the 13 December 2006 CME combining remote sensing and in situ measurements with modeling efforts. A comprehensive view of the CME is made possible by coordinated EUV, coronagraph, radio, particle and in situ plasma and magnetic field observations provided by a fleet of spacecraft including SOHO, STEREO, ACE, Wind and Ulysses.

The CME is accompanied by an X3.4 solar flare, EUV dimmings and EIT waves. It had a speed about 1774 km s^{-1} near the Sun and produced SEP events, radio bursts, an interplanetary shock, and a large ICME embedded with an MC which gave rise to a major geomagnetic storm. The speed of the CME-driven shock is about 1030 km s^{-1} at 1 AU, suggestive of a significant deceleration between the Sun and 1 AU. Reconstruction of the MC with the GS method indicates a flux-rope structure with an axis orientation oblique to the flare ribbons. We observe major SEP events at 1 AU, whose intensities and anisotropies are used to investigate the ICME structure. The ICME is still magnetically connected to the Sun, as indicated by the electron enhancement due to the X1.5 flare within the ICME. Particle deflection and exclusion by the ICME suggest that the energetic particle transport is largely dominated by the transient structures.

The CME-driven shock is also observed at Ulysses while the ICME seems missed. Ulysses was 74° south of the Earth, indicative of a large latitudinal extent of the shock. The shock speed is about 870 km s^{-1} , comparable to its 1 AU counterpart. An MHD model using the 1 AU data as input successfully predicts the shock arrival time at Ulysses with a deviation of only 3.6 hr, substantially smaller than the propagation time 75.1 hr from ACE to Ulysses. The model results also show that the peak solar wind speeds quickly decrease at large distances. Consequently, the CME/shock would not cause large effects in the outer heliosphere.

We draw particular attention to the CME/shock propagation combining coronagraph images, type II bursts, in situ measurements and the MHD model. The height-time profile is deduced from the frequency drift of the type II bands and the shock parameters measured

at 1 AU assuming a kinematic model; uncertainties in the frequency drift are minimized by the constraints from 1 AU data. The shock is tracked remarkably well by the height-time curve, as cross verified by LASCO data, the MHD model output at different distances and Ulysses observations. The CME/shock has a radial speed of 2212 km s^{-1} near the Sun; the effective deceleration is about -34.7 m s^{-2} and lasts for 9.5 hr corresponding to a transit distance of 0.36 AU. These results demonstrate that a shock can be tracked from the Sun all the way to 1 AU (and larger distances) by combining MHD propagation of the solar wind and type II emissions, a technique to predict the shock arrival time with small ambiguities when in situ measurements closer to the Sun are available.

The research was supported by the STEREO project under grant NAS5-03131. We acknowledge the use of SOHO, GOES, ACE, Wind and Ulysses data and CME parameters from the LASCO CME catalogue maintained by NASA and the Catholic University of America in cooperation with NRL. We thank C. T. Russell for helping maintain the STEREO/MAG data. This work was also supported in part by grant NNSFC 40621003.

REFERENCES

- Acuña, M. H., et al. 2007, *Space Sci. Rev.*, doi: 10.1007/s11214-007-9259-2
- Biesecker, D. A., Myers, D. C., Thompson, B. J., Hammer, D. M., & Vourlidas, A. 2002, *ApJ*, 569, 1009
- Cane, H. V., Sheeley, N. R., Jr., & Howard, R. A. 1987, *J. Geophys. Res.*, 92, 9869
- Dungey, J. W. 1961, *Phys. Rev. Lett.*, 6, 47
- Gopalswamy, N., Lara, A., Yashiro, S., Kaiser, M. L. & Howard, R. A. 2001, *J. Geophys. Res.*, 106, 29207
- Gopalswamy, N., et al. 2005, *J. Geophys. Res.*, 110, A09S15
- Hau, L.-N., & Sonnerup, B. U. Ö. 1999, *J. Geophys. Res.*, 104, 6899
- Hu, Q., & Sonnerup, B. U. Ö. 2002, *J. Geophys. Res.*, 107, 1142
- Kahler, S. W., & Reames, D. V. 1991, *J. Geophys. Res.*, 96, 9419
- Kosovichev, A. G., & Sekii, T. 2007, *ApJ*, 670, L147
- Lario, D., et al. 2005, *J. Geophys. Res.*, 110, A09S11

- Larson, D. E., et al. 1997, *Geophys. Res. Lett.*, 24, 1911
- Li, Y., et al. 2007, AGU Fall Meeting, abstract SH32A-0773
- Lin, R. P., Evans, L. G., & Fainberg, J. 1973, *Astrophys. Lett.*, 14, 191
- Lin, R. P., et al. 2008, *Space Sci. Rev.*, in press
- Liu, Y., Richardson, J. D., Belcher, J. W., Kasper, J. C., & Skoug, R. M. 2006a, *J. Geophys. Res.*, 111, A09108, doi:10.1029/2006JA011723
- Liu, Y., Richardson, J. D., Belcher, J. W., Wang, C., Hu, Q., & Kasper, J. C. 2006b, *J. Geophys. Res.*, 111, A12S03, doi:10.1029/2006JA011890
- Liu, Y., Richardson, J. D., Belcher, J. W., & Kasper, J. C. 2007, *ApJ*, 659, L65
- Liu, Y., et al. 2008, *ApJ*, submitted
- Luhmann, J. G., et al. 2007, *Space Sci. Rev.*, doi: 10.1007/s11214-007-9170-x
- Malandraki, O. E., Lario, D., Lanzerotti, L. J., Sarris, E. T., Geranios, A., & Tsiropoula, G. 2005, *J. Geophys. Res.*, 110, A09S06
- McKibben, R. B., et al. 2005, *J. Geophys. Res.*, 110, A09S19
- Mewaldt, R. A., et al. 2007, ICRC, in press
- Müller-Mellin, R., et al. 2007, *Space Sci. Rev.*, doi:10.1007/s11214-007-9204-4
- Mulligan, T., Blake, J. B., & Mewaldt, R. A. 2007, ICRC, in press
- Nelson, G. J., & Melrose, D. B. 1985, in *Solar Radiophysics: Studies of Emission from the Sun at Metre Wavelengths*, ed. D. J. McLean & N. R. Labrum (Cambridge: Cambridge Univ. Press), 333
- Reiner, M. J., Kaiser, M. L., & Bougeret, J.-L. 2001, *J. Geophys. Res.*, 106, 29989
- Reiner, M. J., Kaiser, M. L., & Bougeret, J.-L. 2007, *ApJ*, 663, 1369
- Richardson, J. D., Paularena, K. I., Wang, C., & Burlaga, L. F. 2002, *J. Geophys. Res.*, 107, 1041
- Richardson, J. D., Wang, C., Kasper, J. C., & Liu, Y. 2005, *Geophys. Res. Lett.*, 32, L03S03
- Richardson, J. D., et al. 2006, *Geophys. Res. Lett.*, 33, L23107

- Sauvaud, J.-A., et al. 2007, *Space Sci. Rev.*, doi: 10/1007/s11214-007-9174-6
- Schindler, K., Pfirsch, D., & Wobig, H. 1973, *Plasma Phys.*, 15, 1165
- Sturrock, P. A. 1994, *Plasma Physics: An Introduction to the Theory of Astrophysical, Geophysical and Laboratory Plasmas* (New York: Cambridge Univ. Press), 209
- Thompson, B. J., et al. 1998, *Geophys. Res. Lett.*, 25, 2465
- Viñas, A. F., & Scudder, J. D. 1986, *J. Geophys. Res.*, 91, 39
- Wang, C., Richardson, J. D., & Gosling, J. T. 2000, *J. Geophys. Res.*, 105, 2337
- Wang, C., Richardson, J. D., & Paularena, K. I. 2001, *J. Geophys. Res.*, 106, 13007
- Wang, Y., Zhou, G., Ye, P., Wang, S., & Wang, J. 2006, *ApJ*, 651, 1245
- Zarro, D. M., Sterling, A. C., Thompson, B. J., Hudson, H. S., & Nitta, N. 1999, *ApJ*, 520, L139
- Zhang, J., Li, L., & Song, Q. 2007, *ApJ*, 662, L35



Fig. 1.— Difference images of the CME and source region at different times. Filled in the circle are EIT difference images at 195 Å. Adapted from the LASCO CME catalogue at <http://cdaw.gsfc.nasa.gov>.

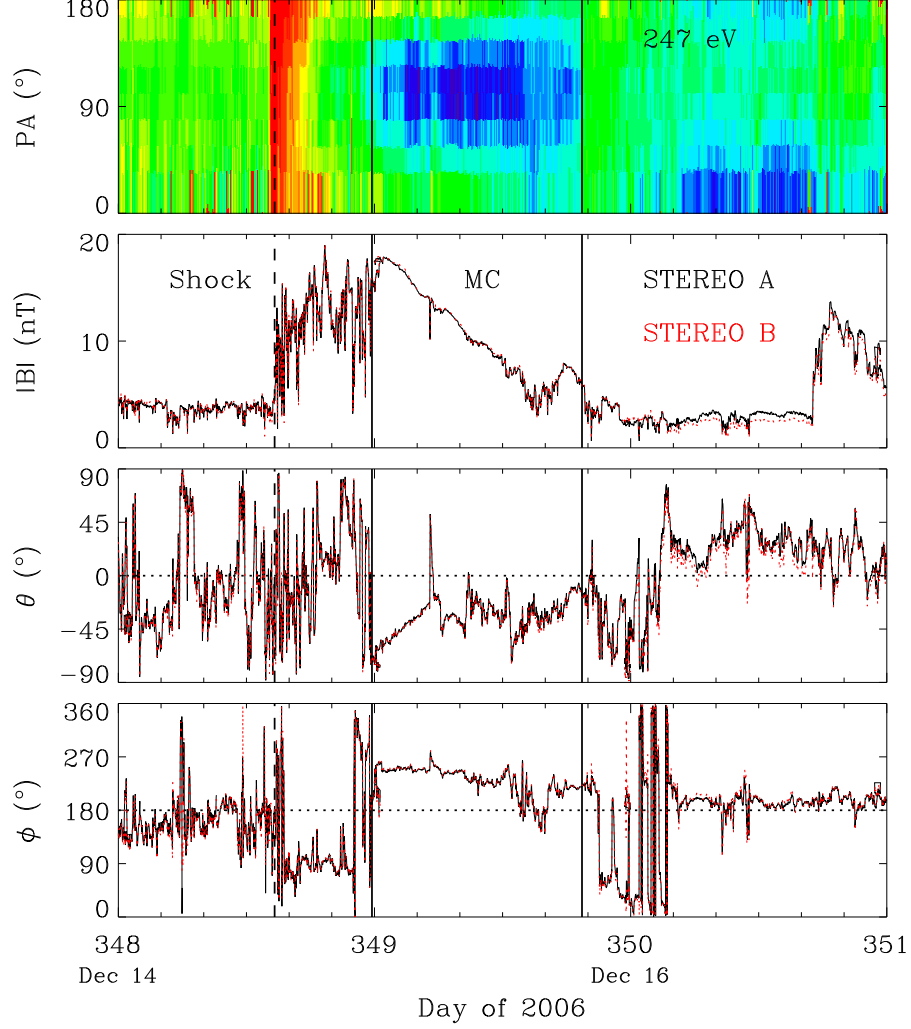


Fig. 2.— STEREO A (black) and B (red) measurements of the pitch angle (PA) distribution of 247 eV electrons, magnetic field strength, and field elevation and azimuthal angles in RTN coordinates across the MC (bracketed by the two vertical lines). The dashed line denotes the arrival time of the MC-driven shock. The color shading indicates values of the electron flux (descending from red to blue).

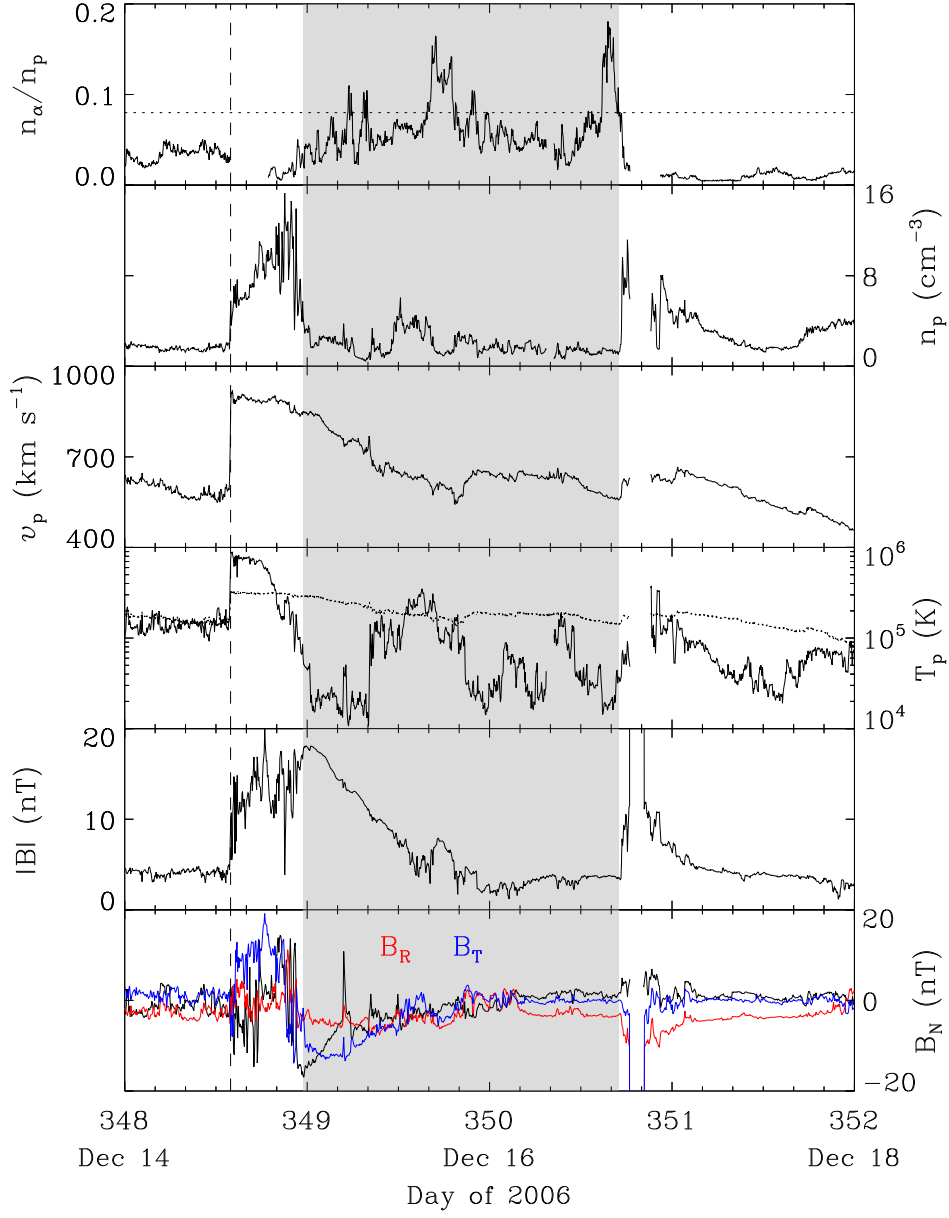


Fig. 3.— Solar wind plasma and magnetic field parameters across the ICME (shaded region) from ACE SWEPAM and MAG. From top to bottom, the panels show the alpha/proton density ratio, proton density, bulk speed, proton temperature, magnetic field strength and components in RTN coordinates. The dotted lines denote the 8% level of the density ratio (first panel) and the expected proton temperature (fourth panel), respectively. The arrival time of the shock is marked by the vertical dashed line.

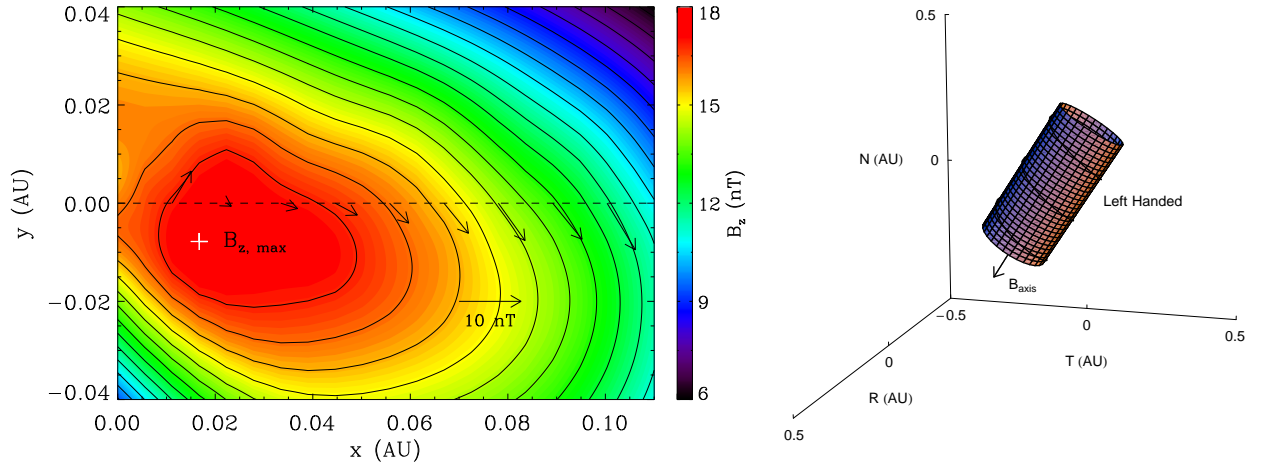


Fig. 4.— Left: Reconstructed cross section of the MC. Black contours show the distribution of the vector potential and the color shading indicates the value of the axial field. The dashed line marks the trajectory of the spacecraft. The arrows denote the direction and magnitude of the observed magnetic fields projected onto the cross section. The location of the maximum axial field is indicated by the plus sign. Right: An idealized schematic diagram of the MC approximated as a cylindrical flux rope in RTN coordinates with the arrow and helical line indicating the field orientation.

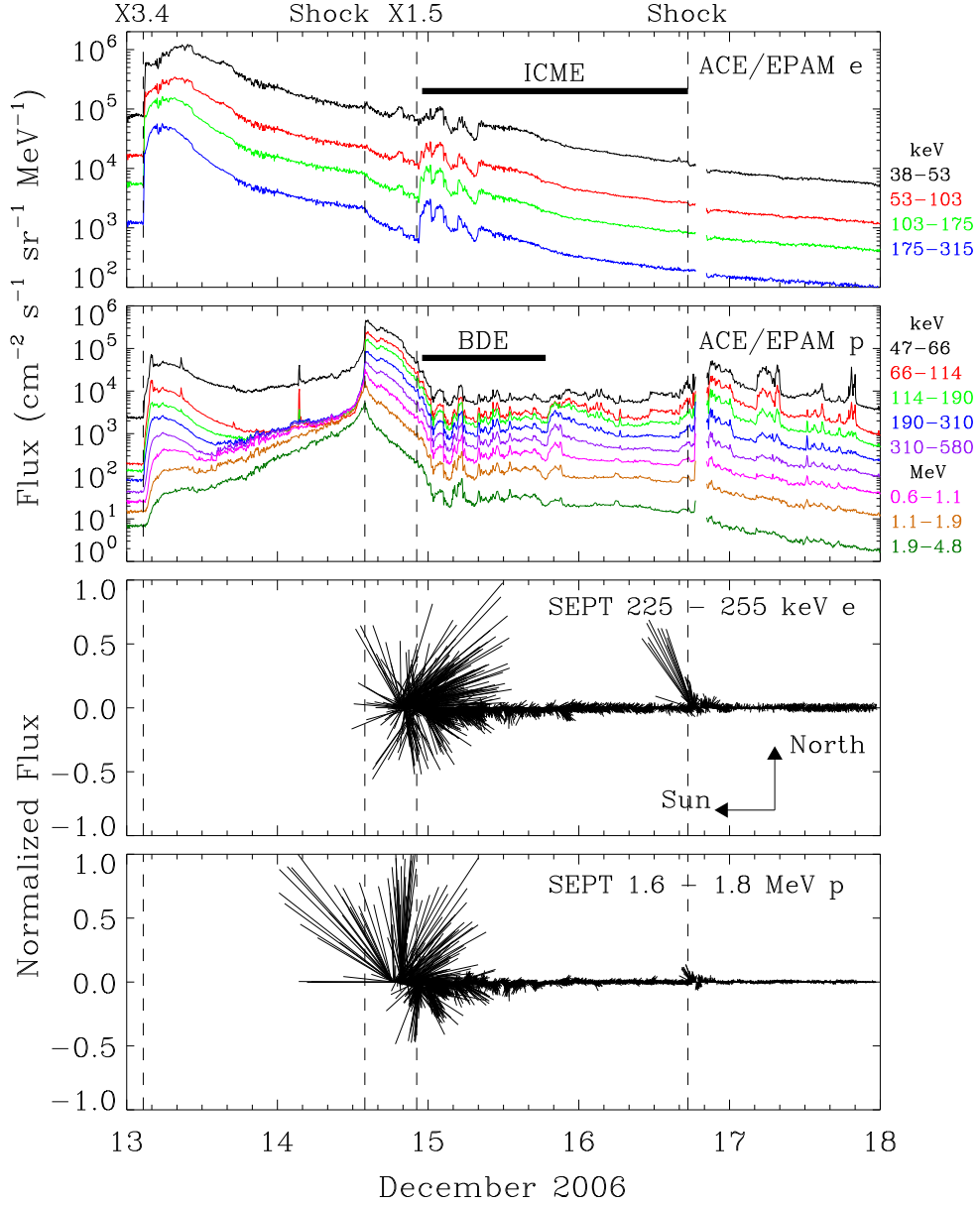


Fig. 5.— Intensities of electrons (top panel) and protons (second panel) at different energy channels measured by ACE/EPAM and anisotropies of electrons (third panel) and protons (bottom panel) observed by STEREO A/SEPT. The times of the flares and shocks are marked by the vertical dashed lines. The ICME and BDE intervals are indicated by the horizontal bars. The solid lines in the two bottom panels denote the normalized intensity differences along the directions defined by the arrows (third panel).

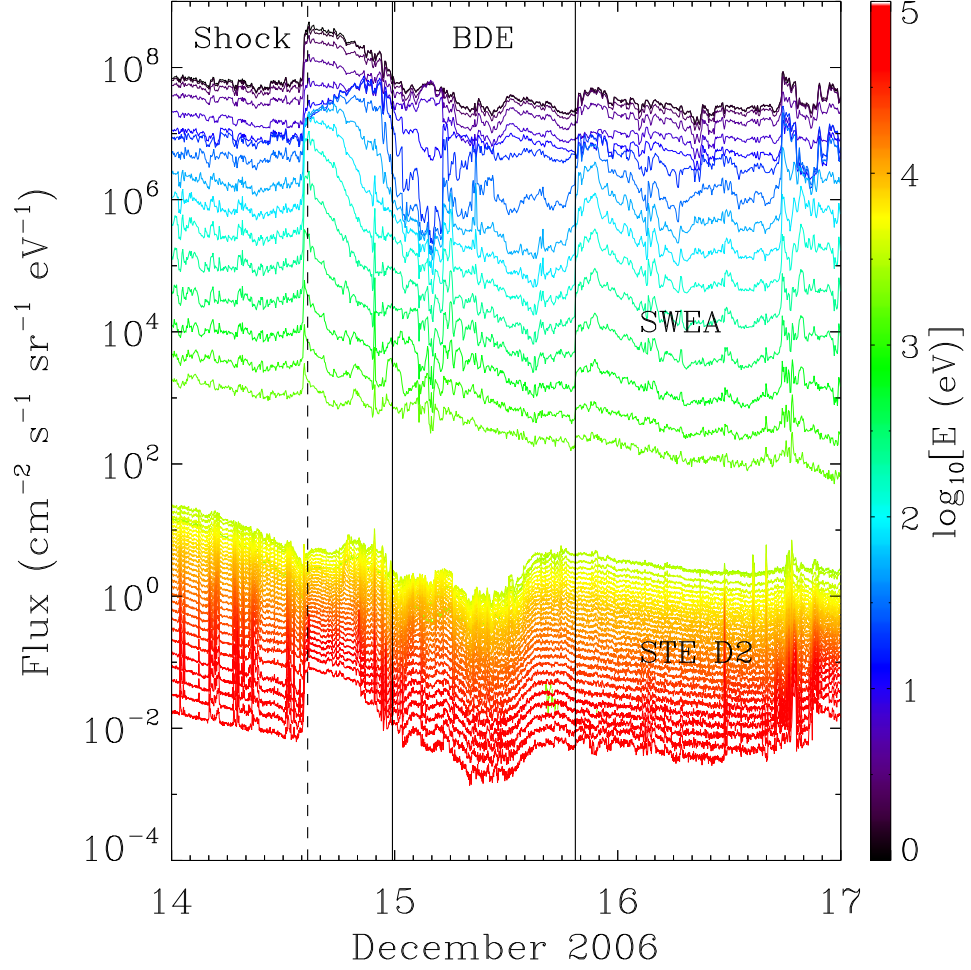


Fig. 6.— Electron intensities across the BDE interval (between the solid lines) measured by SWEA and STE D2 aboard STEREO. The color scale shows the electron energies. The shock arrival time is indicated by the dashed line.

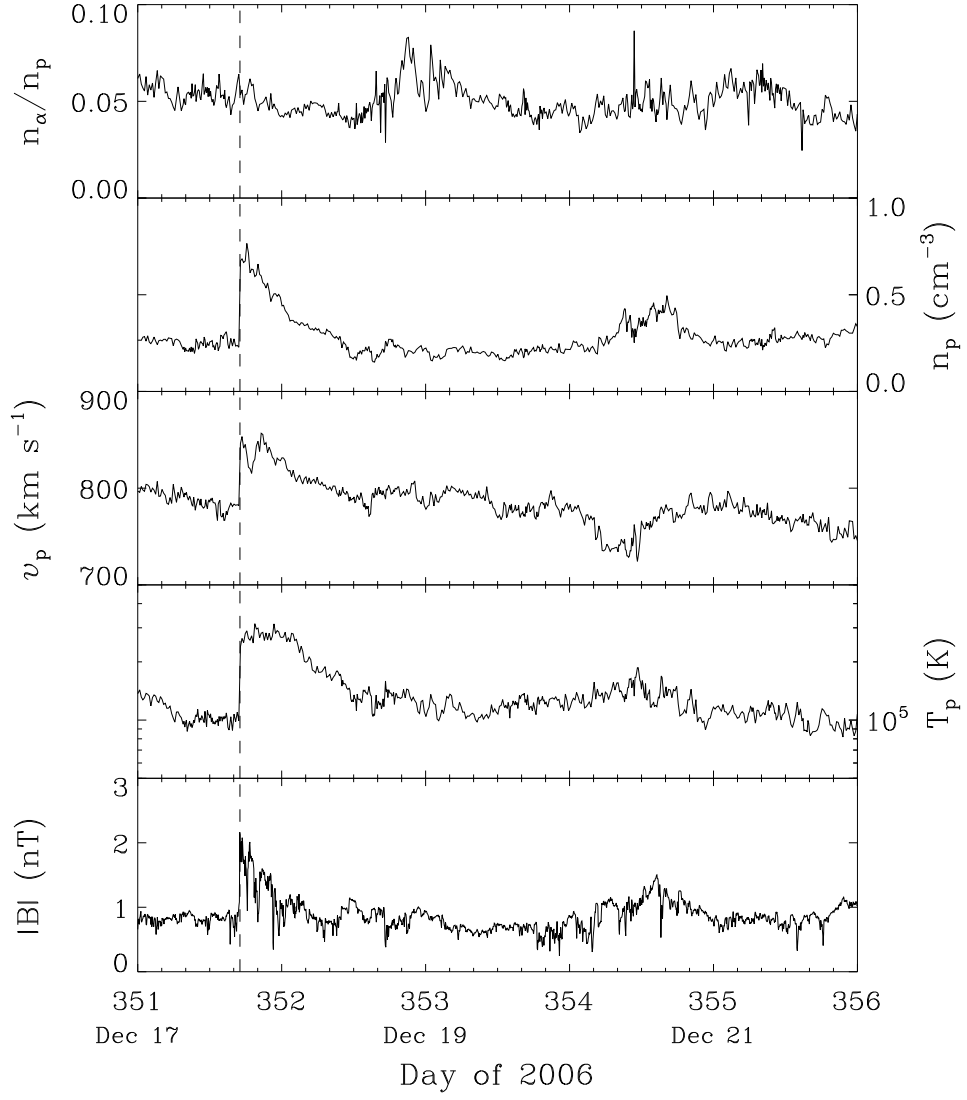


Fig. 7.— Same format as Figure 3, but for the measurements from Ulysses SWOOPS and MFI.

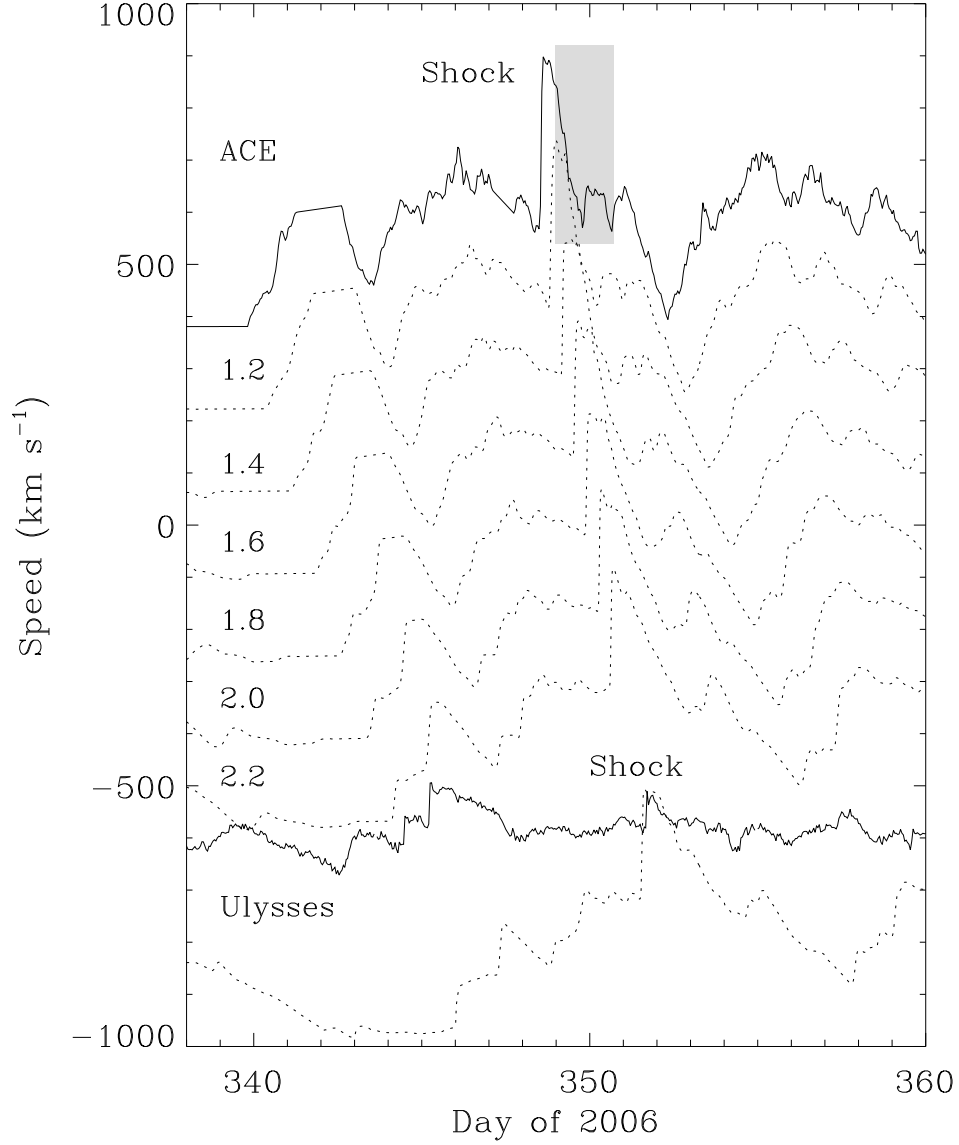


Fig. 8.— Evolution of solar wind speeds from ACE to Ulysses via the MHD model. The shaded region represents the ICME interval at ACE. The upper and lower solid lines show the solar wind speeds observed at ACE and Ulysses. The dotted lines denote the predicted speeds at the distances (in AU) marked by the numbers; each curve is decreased by 160 km s^{-1} with respect to the previous one so that the individual profiles are discernable. The speed profiles at Ulysses (both observed and predicted) are shifted downward by 1360 km s^{-1} from the 1 AU speeds.

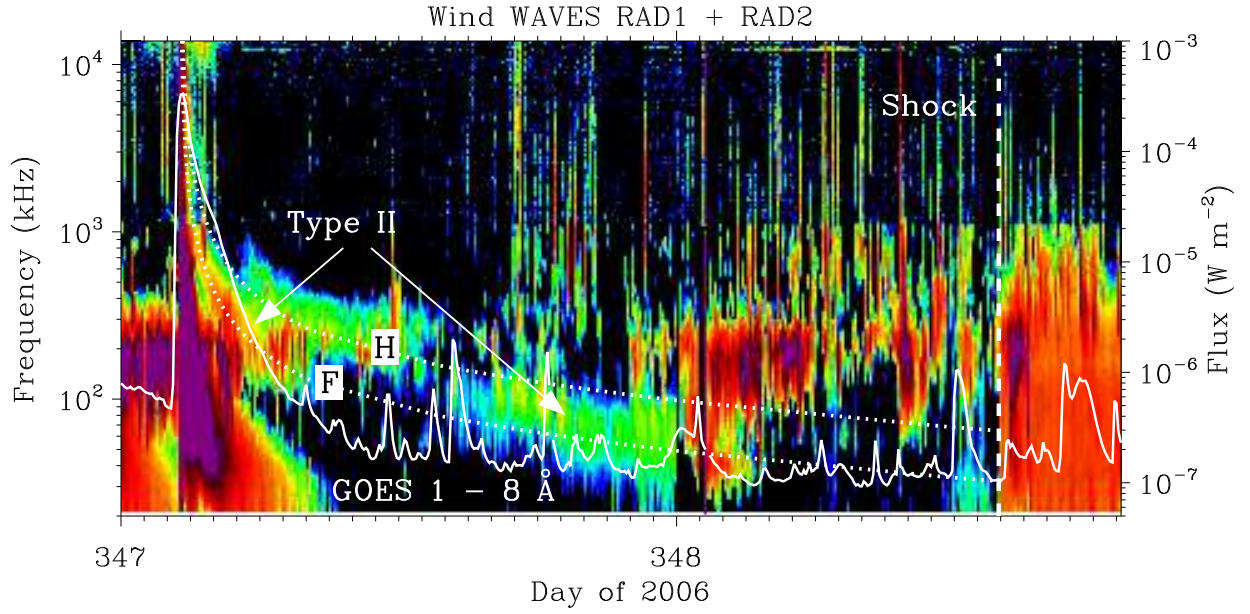


Fig. 9.— Dynamic spectrum (colors) from Wind/WAVES and X-ray flux (solid line) from GOES 12. The dashed vertical line indicates the arrival time of the preceding shock, and the dotted lines represent the best fits of the frequency drift of the fundamental (F) and harmonic (H) type II bursts.

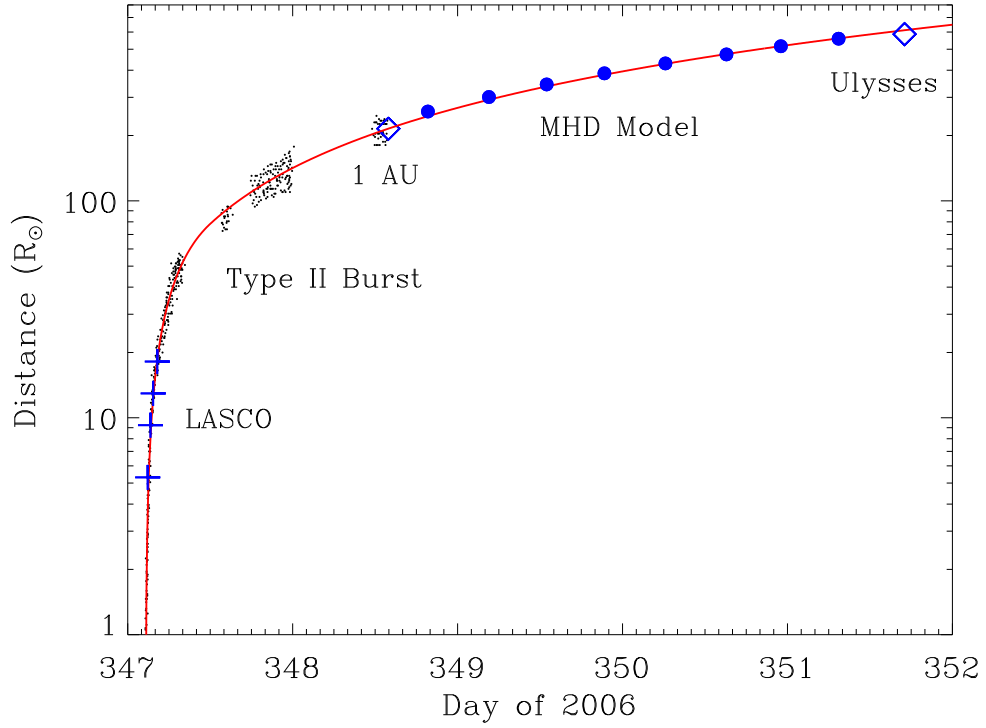


Fig. 10.— Height-time profile (solid line) of shock propagation determined from the frequency drift of the type II bands (dots) and shock parameters measured at 1 AU. Pluses denote the LASCO data. Diamonds indicate the shock arrival times at 1 AU and Ulysses. Between 1 AU and Ulysses are the shock arrival times (filled circles) at [1.2, 1.4, 1.6, 1.8, 2.0, 2.2, 2.4, 2.6] AU predicted by the MHD model.